Applied Catalysis B: Environmental 184 (2016) 77–86

Contents lists available at ScienceDirect

Applied Catalysis B: Environmental

journal homepage: www.elsevier.com/locate/apcatb

Deoxygenation of bio-oil over solid base catalysts: From model to realistic feeds

Begoña Puértolas [1], Tobias C. Keller [1], Sharon Mitchell, Javier Pérez-Ramírez *

Institute for Chemical and Bioengineering, Department of Chemistry and Applied Biosciences, ETH Zurich, Vladimir-Prelog-Weg 1, CH-8093 Zurich, Switzerland

ARTICLE INFO

Article history:
Received 22 September 2015
Received in revised form
14 November 2015
Accepted 16 November 2015
Available online 28 November 2015

Keywords:
Bio-oil deoxygenation
Realistic feeds
Basic zeolites
Hydroxyapatite
Mechanochemical activation

ABSTRACT

This study investigates the design of mild base catalysts for the deoxygenation of bio-oil *via* aldol condensation paths. The first part rationalizes the active, selective, and stable performance of supported MgO catalysts in the vapor phase condensation of propanal, which is maximized upon the mechanochemical activation of a siliceous USY zeolite (Si/Al = 405) with 1 wt.% $Mg(OH)_2$. Infrared spectroscopic studies of the interaction with CO and CO_2, reveal that the presence of 4-coordinate Mg likely localized in framework defects on the zeolite surface, and the avoidance of MgO formation are key to moderating the basicity with respect to the bulk oxide. The second part compares the best-performing MgO/USY catalyst with the most promising previously reported catalysts: K-grafted USY and Ca-hydroxyapatite. A detailed kinetic analysis of the conversion of individual bio-oil constituents (propanal or acetic acid) and binary mixtures thereof (propanal with acetic acid, methanol, or water) provides insights into the reaction network, rate-limiting steps, and relative surface coverage of reactants and products over each catalyst. This enables the anticipation of the aldol-condensation performance in simulated and real bio–oil mixtures. A significant inhibitory effect is observed in the presence of acetic acid, but the K-grafted USY zeolite is found to preserve its stability and retain the highest activity due to the weaker adsorption of acidic compounds. The presence of water has no pronounced effect on the observed reaction rates, while methanol is found to selectively poison Ca-hydroxyapatite due to the competitive adsorption on the active sites. The attained results under real bio-oil conditions demonstrate the effectiveness of this simplified approach to bridge the complexity gap between the study of model compounds and real bio-oil.

1. Introduction

One of the primary challenges in the sustainable production of second-generation biofuels is the development of more efficient routes for the deoxygenation of crude pyrolysis oils (30–50 wt.% oxygen) than the direct hydrodeoxgenation (HDO) or cracking. A promising upgrading strategy comprises a cascade deoxygenation process, wherein the pyrolysis vapors are subjected to catalytic deoxygenation prior to HDO, thereby reducing the H_2 usage by *ca.* 50% [1]. The intermediate step(s) exploit the intrinsic reactivity of the bio-oil constituents to eliminate oxygen as water or carbon oxides *via* condensation reactions as esterification, aldol condensation, and ketonization [2–5]. Aldol condensations are particularly attractive [6], as the low-boiling aldehydes and ketones, which account for up to 25 wt.% of the crude bio-oil [7], can be converted into gasoline- and diesel- range compounds, increasing the yield of liquid fuels and thus, the carbon efficiency. In contrast to traditional strong solid bases such as alkaline earth metal oxides and activated hydrotalcites which prompt rapid deactivation due to the formation of coke [8,9], a number of mild base catalysts have been identified to yield stable performance in aldol condensation such as supported alkali [10,11] or alkaline earth metals [9,12–16], other supported metal oxides [17], and calcium hydroxyapatites [18]. In the case of alkaline earth metal oxides, it is known that the basic strength can be moderated by supporting it on an appropriate material such as SiO_2 [9,12,13], zeolites [14,15] or carbons [16], leading to the weaker bonding of the adsorbed species, and thus facilitating the desorption of the products from the catalyst surface. However, whereas previous studies reported the origin of the moderating effect for supported alkali and calcium hydroxyapatites [11,18], in the case of supported alkaline earth metal catalysts, different synthesis methods, MgO loadings, and types of support have

* Corresponding author. Fax: +41 44 633 1405.
E-mail address: jpr@chem.ethz.ch (J. Pérez-Ramírez).
[1] Equal contribution

http://dx.doi.org/10.1016/j.apcatb.2015.11.017
0926-3373/

been used in each case, leaving the optimal preparation conditions and catalyst composition unclear.

Pyrolysis oils comprise complex mixtures of over 400 different components, 15–35 wt.% water and 0.01–3 wt.% solid particles, which presents significant challenges for the development of catalytic routes for their deoxygenation [19]. Owing to the difficulty in rationalizing the compositional changes based on the individual reaction pathways, and especially the interactions of the different functional groups on the catalyst surface, this is typically approached through the study of model compounds instead of real pyrolysis oils [20]. In particular, for the vapor phase aldol condensation, several studies have been devoted to the investigation of the reaction network for individual aldehydes such as acetaldehyde or butanal over acidic, basic, or bifunctional catalysts either through the *in situ* spectroscopic evaluation [9] or by a full *ex situ* product analysis [4]. Whereas monofunctional (basic) catalysts usually attain a rather simple product distribution [21], for multifunctional materials various side reactions including hydrolysis, cracking, oligomerization, and aromatization [22] are known to compete with aldol condensations, resulting in complex product mixtures consisting of aromatics, linear hydrocarbons, and phenolic compounds among others [23]. However, the mechanistic understanding of the transformation of pure aldehydes in vapor phase is limited [24], and the influence of major bio-oil constituents on the reaction rates remains unaddressed. Accordingly, insights into the interactions of promising catalysts with single bio-oil constituents *versus* complex mixtures can assist in bridging the complexity gap between model components and crude bio-oil.

Herein, we investigate the design of mild base catalysts for bio-oil deoxygenation *via* aldol condensation. To gain insight into the moderate basic strength and performance of supported alkaline earth metal oxides, the first part of the manuscript tackles the preparation of supported MgO catalysts, which is approached by the mechanochemical activation of a high-silica USY zeolite with $Mg(OH)_2$. In-depth characterization provides unprecedented understanding of the nature of the active sites in the resulting MgO/USY catalysts, while their active, selective, and stable performance is confirmed in the self-condensation of propanal. The second part of the manuscript compares the deoxygenation activity of the best-performing MgO/USY with that of previously reported Ca-hydroxyapatite [18], and K-grafted USY catalysts [11]. A comprehensive kinetic analysis of the effect of the addition of representative bio-oil constituents such as acetic acid, methanol, and water on the rate of propanal conversion enables the identification of the mechanistic paths governing the performance of each system in simulated feed mixtures, which is further corroborated under real bio-oil conditions.

2. Experimental

2.1. Catalysts

The parent high-silica USY zeolite (P-USY) was obtained in protonic form from Tosoh Corporation (HSZ-390HUA, Si/Al = 405). MgO/USY zeolites were prepared by dry and wet impregnation, spray deposition, and mechanochemical activation. For the dry impregnation, an aqueous solution (0.25 M, 4 cm^3) of $Mg(NO_3)_2{\cdot}6H_2O$ (99%, Fluka) was added dropwise to the USY zeolite (4 g) at 298 K, which was subsequently dried at 338 K overnight, resulting in sample 1MgO/USY-DI. In the case of wet impregnation, the USY zeolite (4 g) was added to a vigorously stirred aqueous solution of $Mg(NO_3)_2{\cdot}6H_2O$ (0.05 M, 20 cm^3) at 298 K. The resulting mixture was slowly dried in a rotary evaporator (Büchi RE-111) yielding sample 1MgO/USY-WI. The spray deposition method [25] was performed with a Büchi Mini Spray Dryer B-290 equipped with a two-fluid nozzle of 1.4 mm in diameter. The USY zeolite (8 g) was added to a stirred aqueous solution of $Mg(NO_3)_2{\cdot}6H_2O$ (0.025 M, 80 cm^3) at 298 K. The resulting suspension was pumped (3 cm^3 min^{-1}) into the nozzle (T_{inlet} = 493 K, T_{outlet} = 363 K, aspiration rate = 35 m^3 h^{-1}) together with a spray air flow (0.5 m^3 h^{-1}) and the dried powder (1MgO/USY-SD) was separated by a cyclone. For the mechanochemical activation, the zeolite (4 g), the desired amount of $Mg(OH)_2$ (99.9%, Fisher Chemicals), and deionized water (2 cm^3) were milled in a NanBei QM-1SP4 planetary ball mill (500 rpm, 30 min) to reach nominal MgO contents of between 0 and 20 wt.%. The resulting powders (coded *x*MgO/USY, where *x* refers to the nominal MgO content in wt.%), were dried at 338 K. A reference sample subjected to ball milling in the absence of $Mg(OH)_2$ was denoted BM-USY. For comparative purposes, SiO_2 (99.5 wt.%, Sigma–Aldrich) was also used as support (1MgO/SiO_2). All the catalysts were subsequently calcined for 2 h in flowing air at a temperature (T_c) of 873 K unless otherwise specified (heating rate 5 K min^{-1}).

The preparation of the benchmark catalysts, K-grafted USY and Ca-hydroxyapatite, is reported in detail elsewhere [11,18]. Briefly, for the K-USY, the zeolite (2 g) was introduced into a KOH solution (0.1 M, 60 cm^3, 85%, Fisher Chemicals) in methanol (99.8%, Sigma–Aldrich) at room temperature, stirred at 500 rpm for 10 min, filtered, washed thoroughly with the same solvent, dried at 338 K, and subsequently calcined in static air (823 K, 5 h, heating rate 5 K min^{-1}). The calcium hydroxyapatite (coded Ca-HA) was precipitated by the dropwise addition of aqueous $(NH_4)_2HPO_4$ (0.4 M, 98%, Sigma–Aldrich) into a stirred aqueous solution of $Ca(NO_3)_2{\cdot}4H_2O$ (0.6 M, 99%, Sigma–Aldrich) at room temperature and constant pH (9.5), which was adjusted by the addition of ammonia solution (25% in H_2O, Sigma–Aldrich). The precipitate was stirred at the same temperature for 24 h, before it was isolated by filtration, thoroughly washed with deionized water, dried at 383 K for 12 h, and calcined in static air (873 K, 2 h, heating rate 5 K min^{-1}).

2.2. Methods

X-ray diffraction (XRD) patterns were measured on a PANalytical X'Pert PRO-MPD diffractometer using Ni-filtered Cu Kα radiation (λ = 0.1541 nm). Data were recorded in the 2θ range of 5–70° with an angular step size of 0.05° and a counting time of 8 s per step. N_2 and Ar sorption at 77 K were undertaken in Micromeritics TriStar II and Micromeritics 3Flex instruments, respectively. Prior to the measurement, the samples were evacuated at 573 K for 3 h. Fourier transform infrared spectroscopy (FTIR) of adsorbed CO (99.998%, Messer) and CO_2 (99.998%, Messer) were measured in a Bruker IFS 66 spectrometer (650–4000 cm^{-1}, 2 cm^{-1} optical resolution, co-addition of 32 scans). Self-supporting wafers of the sample (5 ton m^{-2}, 50 mg, 1 cm^2) were evacuated to 10^{-3} mbar for 4 h at 693 K, saturated with CO_2 at room temperature, and subsequently evacuated at different temperatures (298–423 K) for 10 min, before the individual spectra were recorded. CO (*ca.* 2 mbar) was adsorbed on the samples at 77 K, followed by evacuation to different pressures, equilibration, and acquisition of the individual spectra. High-angle annular dark field scanning transmission electron (HAADF-STEM) micrographs as well as energy dispersive X-ray spectroscopy (EDS) element maps were acquired on a FEI Talos instrument operated at 200 kV. The samples were dispersed as dry powders onto lacey carbon coated copper grids. As zeolites are known to gradually amorphize upon prolonged exposure to electron radiation, the mapping experiments were typically performed with beam currents of around 70 pA and with a dwell time of 10 ms to further protect the specimen. The magnesium content was determined by inductively coupled plasma optical emission spectroscopy (ICP-OES) on a Horiba Ultima 2 instrument equipped

with a photomultiplier tube detection. Further experimental details are provided in the Supplementary material.

2.3. Catalytic tests

Catalytic tests were carried out at atmospheric pressure in a continuous-flow fixed-bed reactor (12 mm internal diameter) equipped with a Chemyx Fusion 100 classic syringe pump connected to a vaporization line (423 K). In all cases, the catalyst (0.3 g, particle size: 0.2–0.4 mm) was pretreated in He (50 cm^3 min^{-1}) at 723 K for 1 h prior to the reaction. Standard catalyst tests in the self-condensation of propanal were conducted at 673 K. Propanal (99%, Acros Organics) was fed at 1.2 cm^3 h^{-1} in a 50 cm^3 min^{-1} He flow. Similarly, catalytic tests to determine the comparative reaction orders (n_i) in the conversion of single model compounds were conducted at 673 K (Scheme 1). Propanal or acetic acid (99.8%, Sigma–Aldrich) were fed at different rates in a 50 cm^3 min^{-1} He flow to vary the partial pressure of the reactant in the feed. The inhibitory effect of the product in each reaction was studied by co-feeding propanal and 2-methyl-2-pentenal (97%, Acros Organics) or acetic acid and acetone (99.9%, Sigma–Aldrich), respectively in the range 11–18 vol.% for the reaction product. To determine activation energies, the reaction temperature was varied between 623 and 723 K in steps of 25 K. For each catalyst, experiments completed to identify either the reaction order of propanal or the activation energies were performed over the same catalytic bed. An equivalent protocol applies for acetic acid. In all cases, the conversion of either propanal or acetic acid was kept below 20% by decreasing the amount of catalyst. For tests in binary mixtures, propanal was co-fed with acetic acid, water, or methanol (99.7%, Merck) at volumetric ratios between 99:1 and 9:1 at 673 K in a 50 cm^3 min^{-1} He flow. The attained reaction orders $n_{i(P)}$ refer to component i (acetic acid, water or methanol) with respect to the rate of propanal conversion. As for the experiments with single compounds, the same catalyst bed was used for the entire test. For tests in the simulated bio–oil mixture, propanal, acetic acid, water, and methanol were co-fed with a volumetric ratio of 7:1:1:1 at the same temperature and He flow. In all cases, the products were analyzed by an on-line gas chromatograph (HP Agilent 6890) equipped with a flame ionization detector (FID) and a capillary column (HP-5). Conversion (X) and product yields (Y) were calculated based on the integrated peak area of the component of interest, normalized to the total FID response. The reaction rate (r_i) was calculated as the product of the conversion and the total flow of the reactant (i) divided by the catalyst weight. The linear representation of the reaction rate *versus* the propanal partial pressure enables the estimation of the reaction order. The rate constant (k_i) was determined from the quotient between the reaction rate and the partial pressure taking into account the reaction order n_i. Finally, the activation energy ($E_{A,j}$) for the formation of a given product (j) was determined from the slope of the Arrhenius plot using the reaction temperature and respective rate constant. A full description of the kinetic models can be found in the Supplementary material.

The deoxygenation performance of the synthesized catalysts was also tested under real bio-oil conditions. Primary bio-oil was obtained in a bench scale continuous fast pyrolysis unit. Thermal pyrolysis (5 g min^{-1}) of sieved oak wood (*Quercus robur*, 90–500 μm) diluted with silica sand (275 g), was carried out at 773 K using N_2 as a carrier gas. The bio-oil vapors are then cooled and the bio-oil is collected. The catalytic upgrading of bio-oil (1.2 cm^3 h^{-1} in a 50 cm^3 min^{-1} He flow) was carried out in a lab scale plant at a temperature of 673 K, which was measured by a thermocouple located at the top of the catalyst bed. The resulting volatile fraction was passed through an ice trap to collect the upgraded bio-oil. A blank test under the same experimental conditions was also performed to verify the effect of the catalyst on the overall performance. The products attained were divided in three fractions: upgraded bio-oil, solid residue, and non-condensable gases. Additional details on the characterization of the liquid and solid fraction are provided in the Supplementary material.

Table 1
Propanal conversion and selectivity to the aldol condensation products over the MgO/USY zeolites prepared by different methods. Results of the 1MgO/SiO_2 are also included for comparative purposes. Reaction conditions: 0.3 g, 673 K, p_P = 6.25 kPa, 50 cm^3 min^{-1} He flow.

Catalyst	Precursor	T_c (K)	X_p (%)	S_{dimer} (%)	S_{trimer} (%)
1MgO/USY-DI[a]	$Mg(NO_3)_2{\cdot}6H_2O$	873	28	64	7
1MgO/USY-WI[b]	$Mg(NO_3)_2{\cdot}6H_2O$	873	25	70	8
1MgO/USY-SD[c]	$Mg(NO_3)_2{\cdot}6H_2O$	873	27	63	6
1MgO/USY[d]	$Mg(OH)_2$	673	30	74	9
1MgO/USY[d]	$Mg(OH)_2$	773	28	59	7
1MgO/USY[d]	$Mg(OH)_2$	873	24	61	6
1MgO/SiO_2[d]	$Mg(OH)_2$	673	28	57	8

[a] Dry impregnation.
[b] Wet impregnation.
[c] Spray deposition.
[d] Mechanochemical activation.

3. Results and discussion

3.1. Preparation and performance of MgO/USY catalysts

Four key variables were studied in the design of MgO/USY catalysts: the synthetic approach, the MgO content, the calcination temperature, and the catalyst support. A highly siliceous USY zeolite was selected as the parent to avoid the presence of framework aluminum and associated acid sites. In the first instance, samples containing 1 wt.% MgO were prepared by the wet impregnation, dry impregnation, or spray deposition of a magnesium nitrate solution onto the support, or by the solvent-assisted ball milling of the zeolite with $Mg(OH)_2$. In all cases, the metal precursors were subsequently decomposed by calcination at 873 K. The resulting catalysts all evidenced similar textural properties and crystalline order to those of the parent zeolite, and no reflections associated with MgO were visible in the XRD patterns of the calcined materials (results not shown). Evaluation in the vapor phase self-condensation of propanal (Scheme 1 and Table 1) revealed that the synthetic route only had a minor impact on the activity (24–28%) and all of the catalysts exhibit a high selectivity to aldol condensation products (67–78%).

Considering the comparable performance, the subsequent study of the impact of both the calcination temperature (673–873 K) and the metal oxide content (*ca.* 1–20 wt.%) was focused on MgO/USY catalysts prepared by mechanochemical activation, as the most environmentally-benign route. The composition and textural properties of the resulting catalysts are summarized in Table 2. The zeolite was also ball-milled in absence of any Mg precursor to assess the impact of solvent-assisted ball milling on the parent zeolite (BM-USY). While calcination at different temperatures did not impact the structure or porosity of the zeolite, more remarkable reductions of the micropore volume (*ca.* 15–20%) and crystallinity were observed with increasing MgO content. High-resolution Ar sorption at 77 K (Fig. 1) verified that the micropore volume was reduced (10 and 20 wt.%), evidenced by the shift in Ar uptake associated with the micropores to lower relative pressures. These observations are attributed to the presence of MgO agglomerates, which were corroborated by the appearance of characteristic reflections (highlighted in grey) in the XRD patterns of the 10MgO/USY and 20MgO/USY catalysts (Fig. S1).

Consistent with the absence of magnesium, BM-USY exhibited negligible activity in the test reaction. Significant distinctions were observed in the performance of the materials prepared with 1 wt.%

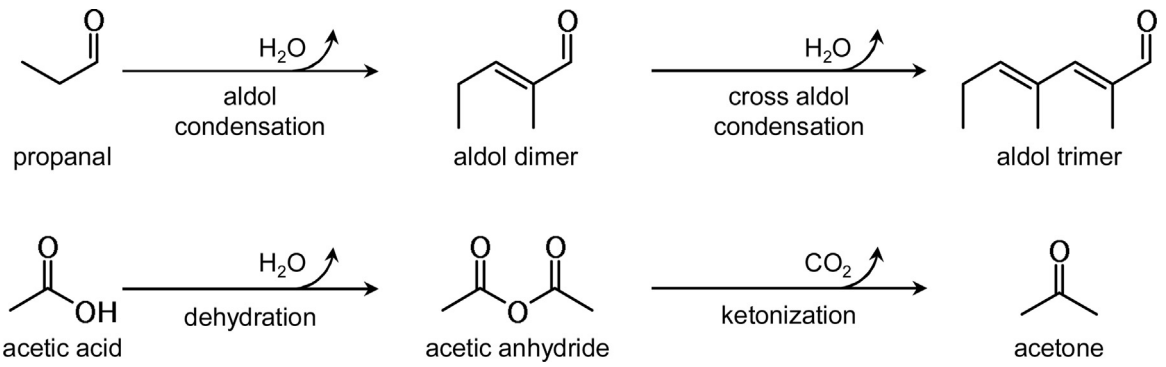

Scheme 1. Reaction pathways for the vapor phase conversion of propanal (top) and acetic acid (bottom) over base catalysts.

Table 2
Overview of catalyst synthesis and characterization data.

Catalyst	Synthesis protocol	Metal[a] (wt.%)	T_c (K)	V_{pore} ($cm^3\ g^{-1}$)	V_{micro}[b] ($cm^3\ g^{-1}$)	S_{meso}[b] ($m^2\ g^{-1}$)	S_{BET}[c] ($m^2\ g^{-1}$)	Crystallinity[d] (%)	Coke[e] (wt.%)
P-USY	Parent USY	–	–	0.56	0.30	117	693	100	–
BM-USY	Mechanoch. activation	–	673	0.53	0.29	112	666	106	–
0.1MgO/USY	Mechanoch. activation	0.07	673	0.60	0.32	121	736	103	2.5
1MgO/USY	Mechanoch. activation	0.98	673	0.51 (0.37, 0.28)[f]	0.25 (0.17, 0.12)	134 (95, 70)	612 (412, 296)	84	4.3 (4.3, 16.5)
1MgO/USY	Mechanoch. activation	1.03	773	0.52	0.25	136	612	84	–
1MgO/USY	Mechanoch. activation	1.06	873	0.52	0.25	136	620	82	–
10MgO/USY	Mechanoch. activation	11.21	673	0.50	0.26	123	613	83	6.7
20MgO/USY	Mechanoch. activation	20.73	673	0.48	0.21	168	575	60	–
K-USY	Grafting	4.60	823	0.51 (0.30, 0.05)	0.27 (0.11, 0)	67 (52, 11)	590 (268, 18)	72	(9.5, 26.1)
Ca-HA	Coprecipitation	1.67	873	0.36 (0.22, 0.19)	0	63 (40, 46)	63 (40, 54)	–	(2.8, 12.4)

[a] MgO, K content or bulk Ca/P ratio ($mol\ mol^{-1}$) determined by ICP-OES.
[b] t-plot method.
[c] BET method.
[d] X-ray diffraction, ASTM standard D3906.
[e] Coke content determined by TGA in the temperature range from 473 to 1103 K.
[f] First values in parenthesis correspond to the used catalysts tested in the simulated bio–oil mixture; second values relate to the used catalysts tested under real bio-oil conditions.

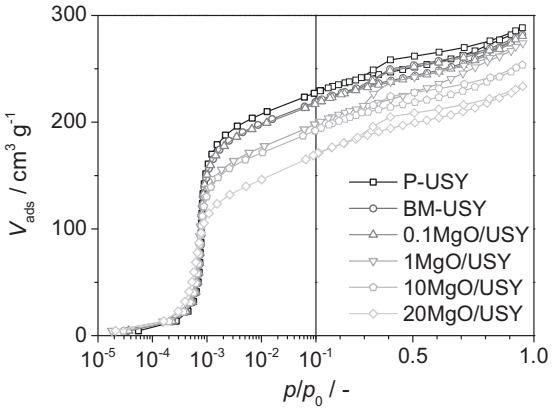

Fig. 1. Ar isotherms at 77 K of MgO/USY zeolites with different MgO content. The isotherms of the parent USY zeolite, and that ball milled in the absence of $Mg(OH)_2$ (BM-USY) are included for comparative purposes.

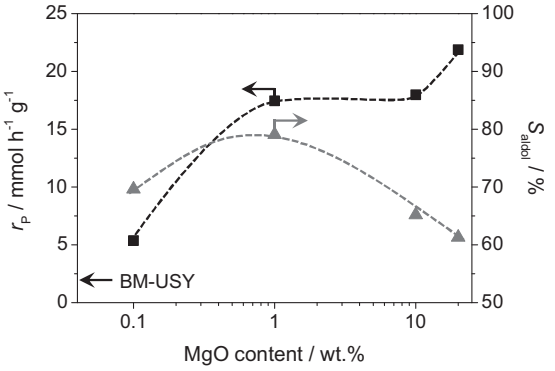

Fig. 2. Rate of propanal conversion (black) and selectivity to the aldol condensation products (grey) *versus* the MgO content over the MgO/USY zeolites. The arrow indicates the rate of propanal conversion over the BM-USY reference. Reaction conditions: 0.3 g, 673 K, p_P = 6.25 kPa, 50 $cm^3\ min^{-1}$ He flow.

MgO on USY and calcined at different temperatures. In particular, decreasing the temperature from 873 to 673 K improved both the conversion of propanal (by 6%) and selectivity to the aldol condensation products (by 15%), and therefore the latter temperature was adopted for further screening. As expected, the rate of propanal conversion increased sharply with increasing MgO content up to 1 wt.%, above which (10 and 20 wt.%) only a marginal activity improvement was attained (Fig. 2). The selectivity to the aldol condensation pathways evidenced a volcano trend reaching a maximum of *ca.* 80% for 1MgO/USY, which is in line with previous observations [26]. In particular, the aldol dimer is predominantly formed while an increasing selectivity to the aldol trimer and other products as 3-pentanone or propene is observed at higher MgO contents (Fig. 3). The latter are formed *via* different reaction pathways [27], and lead to a pronounced increase in the amount of coke deposited in the samples (Table 2). As a result, the catalytic performance remained stable over the 4 h time on stream with a slight deactivation at higher MgO contents (Fig. 3b). The impact of the catalyst support was also evaluated. For similar MgO content and calcination temperature, the selectivity of MgO supported on amorphous SiO_2 to the aldol condensation products was inferior to that observed when USY zeolite is applied as support (65 *versus* 83%).

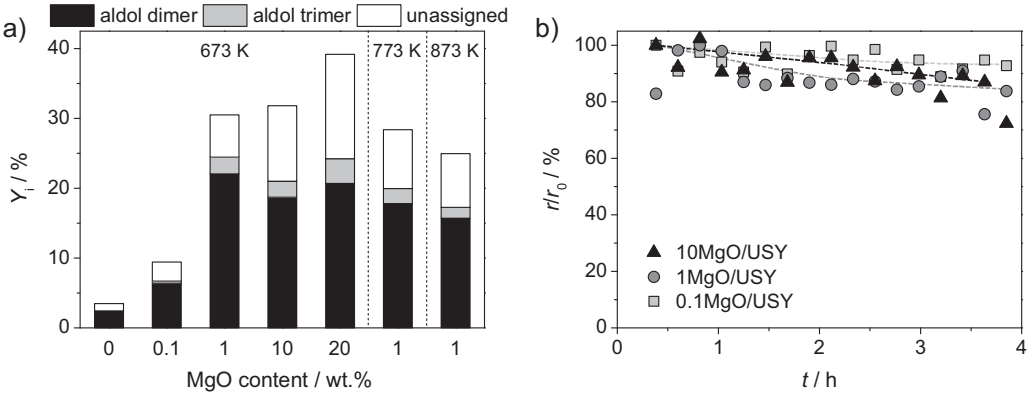

Fig. 3. (a) Product yields and (b) relative decrease in the reaction rate observed in the vapor phase condensation of propanal over MgO/USY zeolites with different MgO content. Catalysts in (a) were calcined at the indicated temperature, while those in (b) were calcined at 673 K. Reaction conditions: 0.3 g, 673 K, p_P = 6.25 kPa, 50 cm^3 min^{-1} He flow.

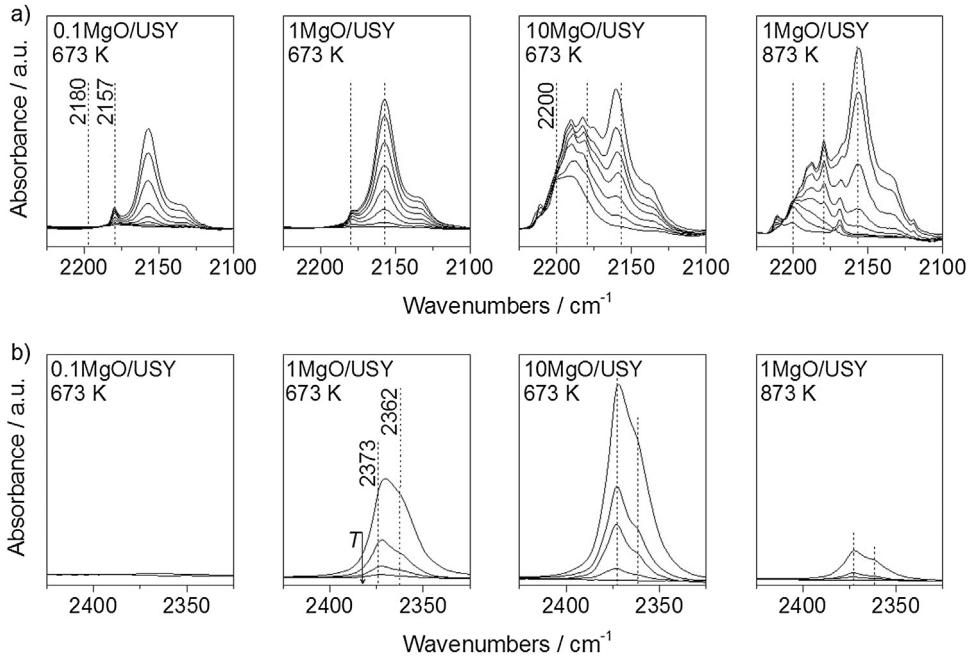

Fig. 4. FTIR spectra after (a) CO adsorption at 77 K (b) CO_2 adsorption at room temperature, and subsequent step-wise desorption over MgO/USY zeolites with different MgO content and calcined at different temperatures. In (a), the bands ascribed to 4-coordinated (2157 cm^{-1}) and 3-coordinated (2180 and 2200 cm^{-1}) Mg^{2+} cations are indicated in each case.

3.2. Basicity assessment of MgO/USY catalysts

To rationalize the performance of the MgO/USY catalysts, the interaction of CO and CO_2 with the activated zeolites was studied in detail by IR-spectroscopy and temperature-programmed desorption experiments, in combination with UV–Vis spectroscopic, and STEM-EDS analyses. As an acidic probe, CO can adsorb on the Mg^{2+} cation, enabling the discrimination between ions with different coordination numbers based on a shift in the IR stretching frequency [28]. In bulk MgO, stronger basic sites are associated with sites of lower coordination, which emerge at steps, edges, and high Miller index surfaces upon thermal removal of water and carbon dioxide between 600–1000 K. As the number of O^{2-} anions (n) coordinated to Mg^{2+} decreases, the signal of CO shifts to higher wavenumbers ($\upsilon_{n=4}$ = 2157 cm^{-1}, $\upsilon_{n=3}$ = 2200 cm^{-1}). Mono-, di-, tri- as well as *iso*-carbonyls can form when CO is adsorbed on alkaline earth metal cations in zeolites depending on the equilibrium pressure and the cation size [29]. Comparison of the IR spectra of the 0.1MgO/USY and 1MgO/USY catalysts measured at 77 K reveals a main band at 2157 cm^{-1} along with a minor contribution at 2180 cm^{-1}, indicating that most of the Mg^{2+} cations coordinate 4 oxygen atoms (Fig. 4). This observation is corroborated by UV–Vis spectroscopy, where contributions characteristic of these sites are observed between 225 and 275 nm (Fig. S2) [30]. In contrast, additional bands are detected at *ca.* 2193 cm^{-1} in the IR spectra of the 10MgO/USY zeolite, which remain upon evacuation. The latter bands are typically associated to the polymerization of CO on the surface of bulk MgO [31]. Indeed, Mg-rich regions likely corresponding to MgO particles are clearly observed by EDS chemical mapping of the 10MgO/USY catalyst. In contrast, a homogeneous distribution of magnesium is observed over the catalyst with a 1 wt.% MgO content (Fig. 5). Previous works [32] indicate that, for small amounts of MgO, the shifts observed (Fig. 4) can be attributed to the nearly stoichiometric crystal surface, *i.e.* defect-free MgO crystals. Nevertheless, although this explanation cannot be fully excluded, it seems improbable given the small crystal size of MgO. Additionally, to the best of our knowledge, no previous works on the study of the surface properties of small MgO clusters

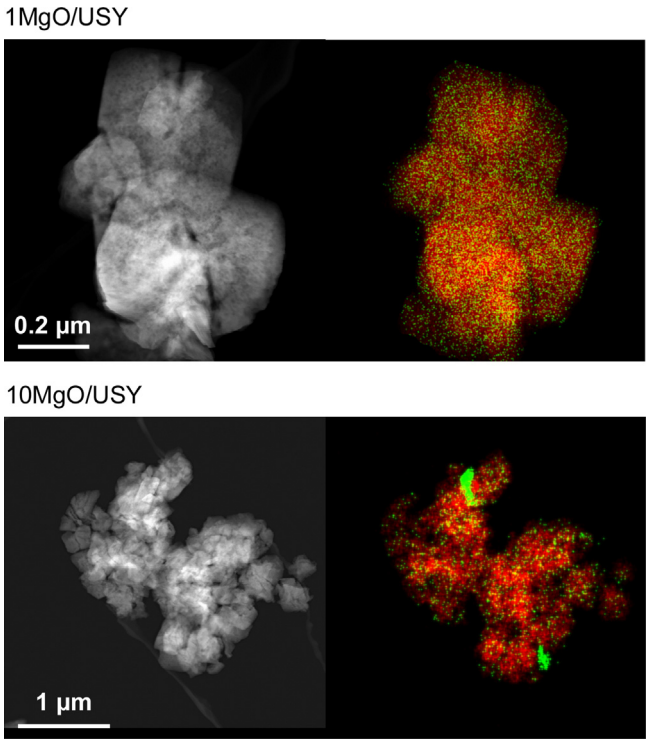

Fig. 5. HAADF-STEM images (left) and elemental maps (right) of Si (red) and Mg (green) of the 1 MgO/USY and 10 MgO/USY zeolite catalysts. The scale bars apply to both images in the same row. (For interpretation of the references to colour in this figure legend, the reader is referred to the web version of this article.)

have been accomplished, which may also interact differently with CO than the bulk oxide. Therefore, in view of the above findings, the nature of the active sites is tentatively attributed to the stabilization of Mg^{2+} cations by defects (*e.g.*, silanol nests or other vacancies) on the surface of the USY zeolite. Due to the finite number of these defects, the introduction of higher quantities of $Mg(OH)_2$ results in the formation of MgO upon calcination. By increasing the calcination temperature, IR spectra evidences a major restructuring of the Mg^{2+} cations, as a higher fraction of 3-coordinate sites is observed at *ca.* 2200 cm^{-1} (Fig. 4). The latter sites, which are minor at lower calcination temperatures, are likely formed due to the dehydration of the 4-coordinate sites and are expected to confer stronger basicity, which is in line with the decrease of the catalytic activity previously described.

The basicity of the catalysts was further assessed by the IR-spectroscopic investigation of adsorbed CO_2 (Fig. 4). Upon saturation with CO_2 and subsequent desorption at room temperature, two main adsorption bands at 2373 and 2362 cm^{-1} were evidenced in all cases, except for the 0.1MgO/USY catalyst. These frequencies should correspond to the asymmetric (υ_3) stretching mode of differently adsorbed CO_2 complexes formed by the interaction with the Mg^{2+} cations [33]. However, as the confinement effect of the zeolite micropores is known to substantially influence the chemical shift of the CO_2 stretching mode, the bands cannot be assigned with more certainty. Upon increasing the desorption temperature, the catalysts containing 1 and 10 wt.% Mg retain CO_2 up to 348 and 373 K, respectively, confirming the higher strength of basic sites in the latter. Additionally, for the catalysts containing 10 and 20 wt.% MgO, the formation of carbonate species in the range of 1600–1800 cm^{-1} is also detected, in line with the presence of MgO in these cases (data not shown). The increase of the basic strength with increasing MgO content is also confirmed by the temperature programmed desorption of CO_2 monitored by gravimetric analysis (Fig. S3a) and chemisorption analysis coupled with mass spectroscopy (Fig. S3b). In the first case, both CO_2 and H_2O are removed from the catalysts during heating, leading to a final weight lower than that registered after the initial evacuation step. This difference was ascribed to water, whereas the remaining corresponds to chemisorbed CO_2. The latter is relatively compared per mole of MgO (0.31, 0.17, and 0.04 mol(CO_2) mol(MgO)$^{-1}$ for 0.1MgO/USY, 1MgO/USY, and 10MgO/USY, respectively) confirming the higher abundance of low-coordinate sites in catalysts with increasing MgO content. Complementary CO_2-TPD experiments ranging from 323 to 973 K confirmed the absence of strong basic sites giving rise to desorption at high temperatures. Upon increasing the calcination temperature, the restructuring of the Mg^{2+} cations was found to reduce the number of basic sites observed, which could be associated with the CO_2 adsorption in the less-coordinated sites, and correspondingly more carbonates were observed. However, due to the temperature limitations of the setup, carbonate species are still observed after evacuation, preventing the discernment of adsorbed CO_2 on these sites.

Finally, the acidic properties of the catalysts were assessed by NH_3-TPD (Fig. S4). As expected, only a very minor NH_3 uptake was observed over BM-USY and 0.1MgO/USY zeolites. Increased uptakes were seen over 1MgO/USY and particularly over 10MgO/USY zeolites evidencing a higher density of acid sites with increasing MgO content, indicating a close relation with the formation of MgO. However, compared to purely acidic materials (*e.g.*, acidic zeolites or silica–alumina), the ammonia uptake of all investigated catalysts is low. Thus, although an influence of neighboring acidic silanols cannot be excluded, the catalytic performance should be mainly governed by the occurrence of mild basic sites.

These findings indicate that the basic sites originating from Mg^{2+} cations likely coordinated with framework defects are the active centers for propanal conversion as the MgO particles formed at higher content yield no catalytic benefit. Thus, in view of its activity and selectivity, the catalyst containing 1 wt.% MgO and calcined at 673 K (hereafter referred to as 1MgO/USY) was selected for the subsequent evaluation in model compound mixtures.

3.3. Kinetic analysis in aldol condensation and ketonization reactions

Apart from selectively catalyzing the conversion of aldehydes *via* aldol condensation paths, solid base catalysts can also efficiently ketonize carboxylic acids, which are prevalent bio-oil constituents. To understand the distinct interaction with mild solid bases, the performance of three of the most promising catalytic systems was evaluated in the conversion of propanal and acetic acid. In particular, the 1MgO/USY zeolite developed in this study was compared with benchmark K-USY and Ca-HA catalysts. In agreement with previous studies [11,18], all of the catalysts exhibited a high activity (Ca-HA > K-USY > MgO/USY) and an excellent selectivity to aldol condensation products (higher than 80%). 1MgO/USY exhibits stable performance over 24 h on stream (Fig. S5) with no significant alteration of its porous and basic properties. No reflections associated with MgO were visible in the XRD patterns of the used catalyst (Fig. S1). The micropore volume decreased by *ca.* 10% of the initial value in all cases. CO_2-TPD results revealed that the strength and density of the mild basic sites is not altered, whereas a new desorption band appears at higher temperatures which could be ascribed to the formation of carbonates during the reaction (Fig. S7a). The stability tests of Ca-HA and K-USY are compiled in previous publications [11,18].

Base-catalyzed aldol condensations are generally expected to follow a four-step reaction mechanism involving (i) the adsorption of the aldehyde on a basic site *via* the α-hydrogen, followed by (ii) the nucleophilic attack of the activated carbonyl by another aldehyde to form the aldol addition product, (iii) the subsequent

Table 3
Kinetic parameters in the reaction of propanal and acetic acid over the selected catalysts.

Reactants	Parameters[a]	1MgO/USY	K-USY	Ca-HA
P	n_P	0.72 ± 0.01	1.01 ± 0.01	1.07 ± 0.08
	$E_{a,D}$ (kJ mol^{-1})	46 ± 2	44 ± 4	80 ± 3
	$E_{a,T}$ (kJ mol^{-1})	102 ± 4	108 ± 10	227 ± 8
H	n_H	0.31 ± 0.05	0.99 ± 0.12	0.30 ± 0.02
	$E_{a,A}$ (kJ mol^{-1})	47 ± 7	80 ± 4	25 ± 2
P + H	$n_{H(P)}$	−0.55 ± 0.06	−0.40 ± 0.05	−0.78 ± 0.02
P + H_2O	$n_{H_2O(P)}$	−0.06 ± 0.08	−0.05 ± 0.03	−0.05 ± 0.03
P + MeOH	$n_{MeOH(P)}$	−0.04 ± 0.01	−0.03 ± 0.01	−0.27 ± 0.04

[a] In binary mixtures, the reaction order refers to acetic acid, water, or methanol with respect to the rate of propanal conversion (P = propanal; D = aldol dimer; T = aldol trimer; H = acetic acid; A = acetone).

elimination of water, and finally (iv) the desorption of the condensation product [34]. While a supporting role of adjacent acid sites for the steps (ii) and (iii) has been reported [35], it is widely accepted that only one basic site is involved in the reaction. In our case, this single site (essentially an Eley-Rideal) mechanism is corroborated by the fact that for the metal-containing USY zeolites, the highest turnover frequencies (TOF) are observed over the materials with the lowest metal contents, *i.e.*, the materials with the most isolated active centers. Indeed, considering that all the Mg incorporated act as active site in the propanal self-condensation, the investigated catalysts exhibit TOF values around 2.5 $mol_{propanal}\ g_{MgO}^{-1}\ h^{-1}$ for the catalysts with 0.1 and 1 wt.% MgO, and around 0.1 $mol_{propanal}\ g_{MgO}^{-1}\ h^{-1}$ for the catalysts with the highest loadings. In contrast, if the reaction proceeded through a dual site (Langmuir-Hinshelwood) mechanism, a volcano-type behavior would be expected for the rate of propanal conversion with respect to the MgO content.

The conversion of propanal and acetic acid over the three catalysts was evaluated at different reactant partial pressures and temperatures to determine the respective reaction order and activation energy for the aldol condensation or ketonization reaction pathways, respectively. The initial performance was subsequently evaluated to corroborate the absence of deactivation over the test period. The resulting values are summarized in Table 3. In the self-condensation of propanal, both K-USY and Ca-HA exhibit a reaction order (n_P) of 1, whereas 1MgO/USY displays a slightly lower reaction order of $n_P = 0.72$ (Fig. 6a). Based on an Eley-Rideal type mechanism (a detailed derivation is provided in the Supporting material), a reaction order of 1 can occur if either the surface reaction or the desorption equilibrium of the reaction product are the rate-limiting steps. The latter can be simply discriminated by co-feeding the reaction product. If the surface reaction is rate limiting, the catalyst surface should be fully covered with the adsorbed educt, and consequently no impact on the reaction rate would be expected. In contrast, if the desorption is the rate-limiting step, the reaction rate should be reduced, as the surface would be partially covered with dimer and trimer products. For the K-USY catalyst, the introduction of 2-methyl-2-pentenal (11–18 vol.%) did not significantly impact the propanal conversion (Fig. 6a, full symbols), indicating that the surface reaction is the rate-limiting step. Conversely, the reaction rate decreased to *ca.* 63% of the initial conversion over the 1MgO/USY and to *ca.* 54% over Ca-HA, indicating that the desorption of the dimer is the rate-limiting step over these catalysts.

When reacting *via* aldol condensation, propanal is initially converted to the 2-methyl-2-pentenal dimer, but can undergo further couplings to form the aldol trimer (Scheme 1). Determination of the activation energy for the formation of the aldol dimer (Fig. 6b), revealed that while K-USY and 1MgO/USY zeolite catalysts exhibited similar values, approximately double the energy was required for the Ca-HA catalyst. Moreover, the energy barrier for the formation of the aldol trimer is also much higher than that to form the aldol dimer, which is in line with the lower yield of secondary reaction products previously observed (Fig. 3a, [11,18]).

As observed for the self-condensation of propanal, the ketonization of acetic acid likely follows a single site Eley-Rideal mechanism. Nevertheless, comparatively different trends are observed in the latter reaction. A reaction order (n_H) of *ca.* 1 was evidenced over the K-USY zeolite catalyst, while a lower reaction order of *ca.* 0.3 was observed over the 1MgO/USY zeolite and Ca-HA catalysts (Table 3), indicating that product desorption is the controlling step in the latter systems and consequently high surface coverages of acetone can be expected. Based on the reaction order of K-USY, both the surface reaction and/or the desorption of the acetone product could be the rate-limiting steps. However, the detrimental impact of co-feeding acetone on the ketonization of acetic acid (Fig. 6b, full symbols), suggests that acetone desorption is the limiting step. The activation energies decrease in this order: K-USY > 1MgO/USY > Ca-HA, indicating that the ketonization is less favored over the K-grafted USY zeolite catalyst, which could have major implications in the next step when the impact of mixtures of increasing complexity on the deoxygenation performance is evaluated.

3.4. Kinetic analysis in multicomponent mixtures

After determining the kinetic parameters in the conversion of pure feeds, the influence of the presence of other bio-oil constituents on the aldol condensation was studied by co-feeding acetic acid, water, or methanol (1–10 vol.%, Fig. 7) with propanal. The reaction order of each compound with respect to the rate of propanal conversion ($n_{i(P)}$) is summarized in Table 3. Acetic acid was found to have the strongest inhibitory effect, which can be understood on the basis of the competitive adsorption expected due to the strong interaction of this acid with the basic centers. Indeed, the most significant impact was observed over the Ca-HA and 1MgO/USY catalysts, for which product desorption was identified as rate-limiting in both the aldol condensation and ketonization reactions, while the effect was slightly less pronounced over the K-USY zeolite. Consistent with the lower reaction orders evidenced in the conversion of the pure compound, the active centers of the former catalysts are expected to be covered with acetic acid and its reaction product to a larger extent compared to K-USY, thus limiting the number of sites available for propanal condensation. The co-feeding of water only resulted in a minor decrease in catalyst activity (Fig. 7b) over all catalysts. This can be expected in view of the fact that all of the systems exhibit a stable conversion of in the self-condensation of propanal in which water is stoichiometrically formed as a by-product (Scheme 1). Upon co-feeding methanol, K-USY and 1MgO/USY exhibited a comparable aldol condensation performance, whereas a significant inhibitory effect was observed in the case of Ca-HA. Calcium hydroxyapatite is a well-known catalyst for the Guerbet coupling of alcohols [36,37], and thus methanol can be expected to interact strongly with the surface.

Finally, the performance of the catalysts was compared under the simultaneous addition of the four investigated bio-oil constituents to simulate a real bio-oil (Fig. 8a). Consistent with the strong inhibitory effect of acetic acid evidenced in the study of binary mixtures, a dramatic decrease in the conversion of propanal was observed over the 1MgO/USY and Ca-HA catalysts. In contrast, the K-USY zeolite catalyst exhibited a stable performance, retaining *ca.* 20% of the initial activity under these conditions (Fig. 8b). K-USY and 1MgO/USY recovered their initial performance on reverting to the original feed (Fig. 8a), which suggests that the catalyst structure was not majorly altered by the other components. TGA analysis of the used catalysts (Table 2 and Fig. S6) revealed that a higher amount of coke was deposited in K-USY compared to 1MgO/USY,

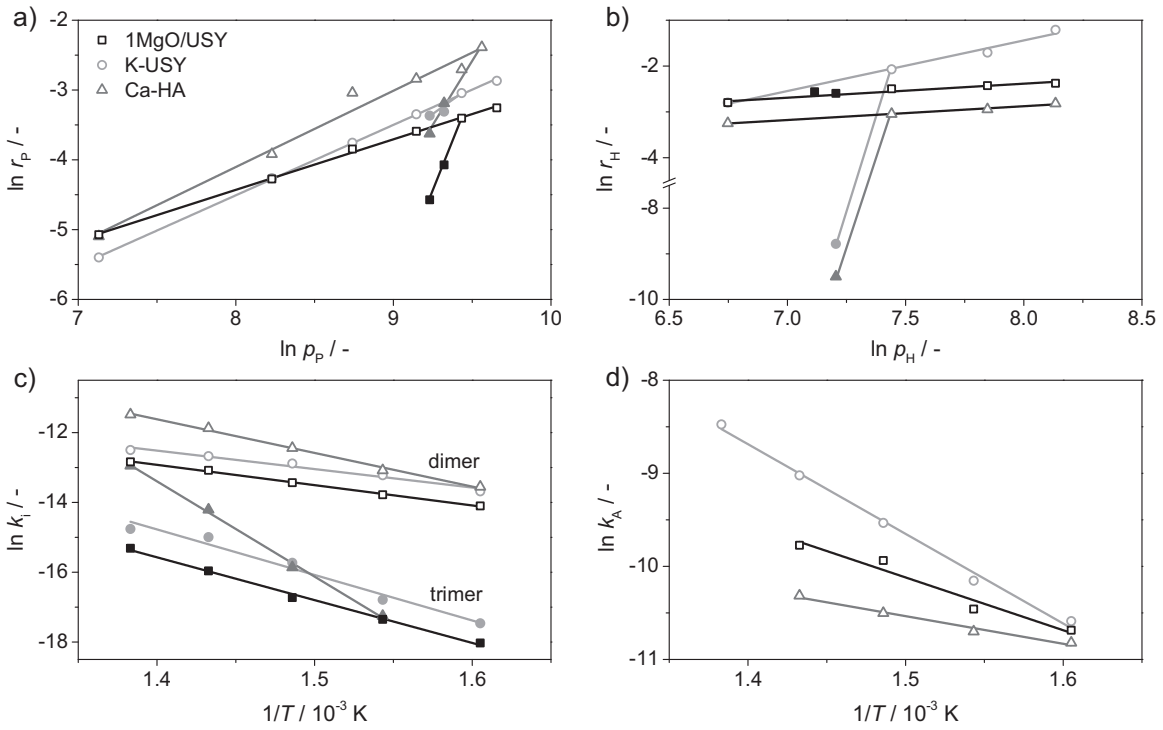

Fig. 6. Reaction rate *versus* the partial pressure of (a) propanal and (b) acetic acid observed over the selected catalysts (open symbols), and while introducing 11–18 vol.% of the respective reaction product (full symbols). Arrhenius plots for the formation of (c) the aldol condensation dimer and trimer (denoted as i), and (d) of acetone.

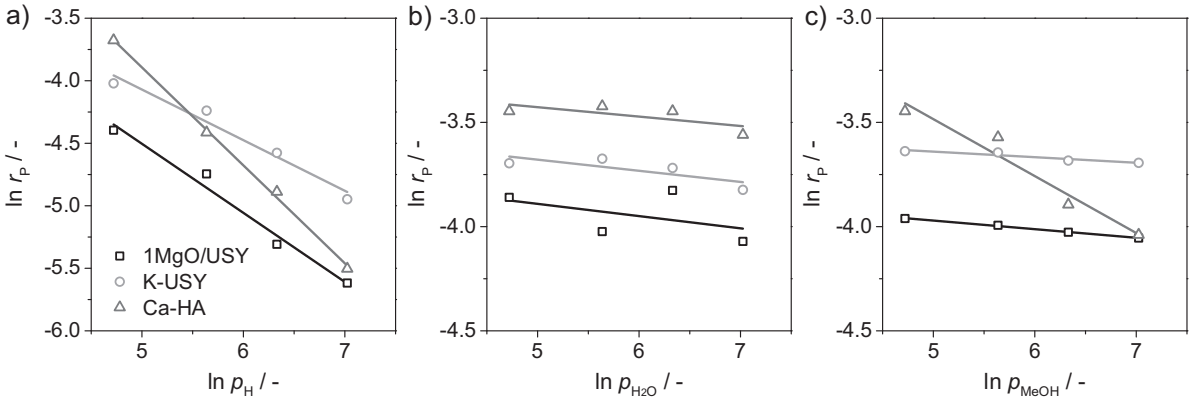

Fig. 7. Impact of co-feeding (a) acetic acid, (b) water, and (c) methanol on the rate of propanal conversion over the selected catalysts. Reaction conditions: 0.3 g, 673 K, 50 cm^3 min^{-1} He flow.

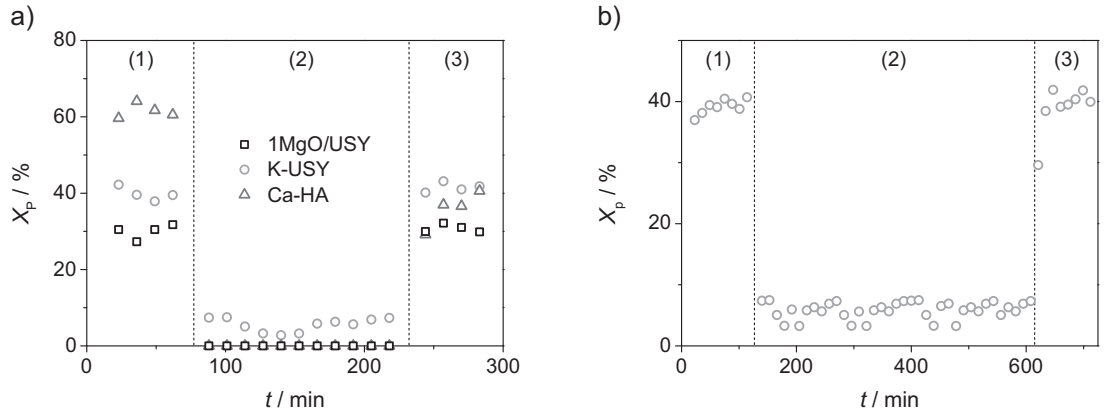

Fig. 8. (a) Conversion of propanal over the selected catalysts and (b) stability test of K-USY feeding 1.2 cm^3 h^{-1} of (1) propanal, (2) a simulated bio–oil mixture containing propanal, acetic acid, water, and methanol with a volumetric ratio of 7:1:1:1, and (3) propanal. Reaction conditions: 0.3 g, 673 K, 50 cm^3 min^{-1} He flow.

in agreement with the more significant decrease in porosity. However, for the Ca-HA catalyst the conversion decreased by *ca.* one third, but recovered with prolonged time on stream, most likely due to the progressive desorption of strongly adsorbed substrates. Further characterization by N_2 sorption and CO_2-TPD (Table 2 and Fig. S7) revealed only a minor textural alteration compared to the fresh catalyst, thus supporting the partial blockage of the active sites as the main reason for the reduced performance. The detrimental influence of the other bio-oil constituents, most likely acetic acid, can be attributed to the competitive chemisorption of the educts and reaction products on the active sites. This implies that an efficient bio-oil deoxygenation catalyst should have zero surface coverage under operation conditions, and thus catalysts with even milder basic sites than the materials investigated herein need to be developed.

3.5. Deoxygenation performance under real bio-oil conditions

The performance of the catalysts was finally evaluated under real bio-oil conditions. The bio-oil was obtained from oak wood in a fast pyrolysis unit. The product distribution and elemental analysis of the upgraded bio-oil are detailed in Tables S1 and S2, respectively. Herein, the accurate identification of the different products leads to a mass balance with an accuracy of *ca.* ±1.9%. In the case of Ca-HA, the product distribution is similar to that attained in the blank experiment, whereas 1MgO/USY and K-USY both exhibit a higher gas yield (*ca.* 24 wt.%). In the case of K-USY, this increase occurs at the expense of the decrease in the liquid yield, whereas for 1MgO/USY, a decrease in the solid yield is detected. TGA analysis of the used catalysts (Table 2 and Fig. S6) revealed that a higher amount of coke was deposited in K-USY compared to 1MgO/USY and Ca-HA, in agreement with the largest reduction in porosity. Analysis of the oxygen content shown in Table S2, reveals a reduction of 15.2, 24.7, and 16.9% for 1MgO/USY, K-USY, and Ca-HA, respectively, which is in line with the experimental trend observed for the activity of these catalysts with the simulated bio-oil mixture, thus supporting the validity of our approach to bridge the complexity gap between model compounds and real bio-oil. Characterization of the used catalysts reveals a severe reduction in the concentration of basic sites in all cases, most likely due to catalyst poisoning by bio-oil constituents or residual particles (char, ash) from the thermal pyrolysis in the bio-oil. Further studies assessing the stability of the synthesized materials jointly with an optimization of the reaction conditions to favor deoxygenation reactions need consideration to enable the efficient production of second-generation biofuels.

4. Conclusions

In this study, we have rationalized the active, selective, and stable performance of supported MgO catalysts in the model self-condensation of propanal. Characterization by the IR study of the interaction with CO and CO_2, CO_2-TPD, XRD, and chemical mapping by STEM, revealed that the moderation of the basic strength is favored by the high dispersion of small amounts of MgO on siliceous USY zeolites prepared by mechanochemical activation, which is ascribed to the incorporation of Mg^{2+} into framework defects on the zeolite surface. The finite number of these defects leads to the formation of undesirable MgO side phases with increasing Mg content, which promote the unselective conversion of propanal due to their strong basicity. Subsequently, the deoxygenation performance of the best-performing catalyst *via* aldol condensation was benchmarked against Ca-hydroxyapatite and K-USY zeolite catalysts, two of the most promising previously reported systems. The assessment of the impact of other representative bio-oil constituents, such as carboxylic acids, alcohols, and water revealed that acetic acid had the strongest inhibitory effect on the reaction rate. Nevertheless, the investigated potassium-grafted USY zeolites, in which such acidic compounds are weakly adsorbed, retained the largest fraction of their activity, as well as their stability. Water and methanol did not affect the performance of the alkali or alkaline earth metal-containing zeolite catalysts, whereas the acid-base bifunctional calcium hydroxyapatite evidenced a strong reduction in the presence of methanol due to the competitive adsorption on the active sites. Based on the kinetic analysis of the attained results with single model compounds of bio-oil and mixtures thereof, an improved mechanistic understanding was accomplished, which enables the rationalization of the deoxygenation performance of mild base catalysts under more realistic conditions. This simplified approach assists in bridging the complexity gap between model reactions and real feeds, which is further corroborated under bio-oil conditions, representing a major step towards the development of economically viable processes for the production of second generation biofuels.

Acknowledgements

This work was funded by ETH Zurich ETH-31 13-1) and the European Union Seventh Framework Programme (FP7/2007–2013) under grant agreement no. 604307. The Scientific Center for Optical and Electron Microscopy (ScopeM) at ETH Zurich is thanked for use of the facilities. The Micromeritics Grant Program is thanked for the award of the 3Flex instrument. The authors would like to thank Dr. E. Heracleous and Prof. A. Lappas from CPERI/CERTH for providing them with the bio-oil samples.

Appendix A. Supplementary data

Supplementary data associated with this article can be found, in the online version, at http://dx.doi.org/10.1016/j.apcatb.2015.11.017.

References

[1] CASCATBEL project, www.cascatbel.eu (last accessed on 21.07.15.).
[2] L. Ciddor, J.A. Bennett, J.A. Hunns, K. Wilson, A.F. Lee, J. Chem. Technol. Biotechnol. 90 (2015) 780–795.
[3] M. Milina, S. Mitchell, J. Pérez-Ramírez, Catal. Today 235 (2014) 176–183.
[4] X. Zhu, L.L. Lobban, R.G. Mallinson, D.E. Resasco, J. Catal. 271 (2010) 88–98.
[5] C.A. Gärtner, J.C. Serrano-Ruiz, D.J. Braden, J.A. Dumesic, ChemSusChem 7 (2014) 1729–1738.
[6] J.N. Chheda, J.A. Dumesic, Catal. Today 123 (2007) 59–70.
[7] D. Mohan, C.U. Pittman Jr., P.H. Steele, Energy Fuels 20 (2006) 848–889.
[8] J.I. Di Cosimo, C.R. Apesteguía, J. Mol. Catal. A: Chem. 130 (1998) 177–185.
[9] W. Shen, G.A. Tompsett, R. Xing, W.C. Conner Jr., G.W. Huber, J. Catal. 286 (2012) 248–259.
[10] T.C. Keller, E.G. Rodrigues, J. Pérez-Ramírez, ChemSusChem 7 (2014) 1729–1738.
[11] T.C. Keller, K. Desai, S. Mitchell, J. Pérez-Ramírez, ACS Catal. 5 (2015) 5388–5396.
[12] C. Angelici, M.E.Z. Velthoen, B.M. Weckhuysen, P.C.A. Bruijnincx, ChemSusChem 7 (2014) 2505–2515.
[13] R. Sundararaman, C. Song, Appl. Catal., B 148–149 (2014) 80–90.
[14] N. Jiang, H. Jin, E.-Y. Jeong, S.-E. Park, J. Nanosci. Nanotechnol. 10 (2010) 227–232.
[15] P. Kovacheva, K. Arishtirova, S. Vassilev, Appl. Catal. A (2001) 391–395.
[16] A.M. Frey, S.K. Karmee, K.P. de Jong, J.H. Bitter, U. Hanefeld, ChemCatChem 5 (2013) 594–600.
[17] W. Ji, Y. Chen, H.H. Kung, Appl. Catal. A 161 (1997) 93–104.
[18] E.G. Rodrigues, T.C. Keller, S. Mitchell, J. Pérez-Ramírez, Green Chem. 16 (2014) 4870–4874.
[19] Q.A. Lu, Z.F. Zhang, C.Q. Dong, X.F. Zhu, Energies 3 (2010) 1805–1820.
[20] M. Asadieraghi, W.M.A.W. Daud, H.F. Abbas, Renewable Sustain. Energy Rev. 36 (2014) 286–303.
[21] G. Zhang, H. Hattori, K. Tanabe, Appl. Catal. 36 (1988) 189–197.
[22] E.L. Kunkes, E.I. Gürbüz, J.A. Dumesic, J. Catal. 266 (2009) 236–239.
[23] B. Puértolas, A. Veses, M.S. Callén, S. Mitchell, T. García, J. Pérez-Ramírez, ChemSusChem 8 (2015) 3283–3293.
[24] Y.-C. Chang, A.-N. Ko, Appl. Catal. A 190 (2000) 149–155.

[25] R. Stevens, L. Vanmarche, R. Elderson, US Pat. 7704420 B2, 2010.
[26] P. Kovacheva, N. Davidova, A.H. Weiss, Stud. Surf. Sci. Catal. 82 (1994) 403–409.
[27] T.C. Keller, S. Isabettini, D. Verboekend, E.G. Rodrigues, J. Pérez-Ramírez, Chem. Sci. 5 (2014) 677–684.
[28] G. Spoto, E.N. Grivob, G. Ricchiardi, A. Damin, D. Scarano, S. Bordiga, C. Lamberti, A. Zecchina, Prog. Surf. Sci. 76 (2004) 71–146.
[29] K. Hadjiivanov, H. Knözinger, J. Phys. Chem. B 105 (2001) 4531–4534.
[30] A. Zecchina, M.G. Lofthouse, F.S. Stone, J. Chem. Soc. Faraday Trans. 1 (71) (1975) 1476–1490.
[31] A. Zecchina, S. Coluccia, G. Spoto, D. Scarano, L. Marchese, J. Chem. Soc. Faraday Trans. 86 (1990) 703–709.
[32] G. Pacchioni, Nanocatalysis, in: U. Heiz, U. Landman (Eds.), Springer, Inc., New York, 2008, pp. 193–243.
[33] P. Nachtigall, M.R. Delgado, D. Nachtigallova, C.O. Orean, Phys. Chem. Chem. Phys. 14 (2012) 1552–1569.
[34] I. di Cosimo, Aldol Reaction—Heterogeneous, Encyclopedia of Catalysis, John Wiley & Sons, Inc., 2010.
[35] R.K. Zeidan, M.E. Davis, J. Catal. 247 (2007) 379–382.
[36] T. Tsuchida, J. Kubo, T. Yoshioka, S. Sakuma, T. Takeguchi, W. Ueda, J. Catal. 259 (2008) 183–189.
[37] J.T. Kozlowski, R.J. Davis, ACS Catal. 3 (2013) 1588–1600.